

Isogeometric nonlinear shell elements for thin laminated composites based on analytical thickness integration

Farshad Roohbakhshan and Roger A. Sauer ¹

Aachen Institute for Advanced Study in Computational Engineering Science (AICES), RWTH Aachen University, Templergraben 55, 52056 Aachen, Germany

Published² in *Journal of Micromechanics and Molecular Physics*,
DOI: [10.1142/S2424913016400105](https://doi.org/10.1142/S2424913016400105)

Submitted on 04. November 2016, Accepted on 07. November 2016, Published on 06. December 2015

Abstract: This paper presents two different formulations for the modeling of thin laminated composite shells, which do not need any numerical integration through the shell thickness. The two proposed formulations are suitable for thin rotation-free shells based on Kirchhoff–Love kinematics. The composite shell is modeled in the framework of equivalent single layer (ESL) theory and the kinematics are adopted from classical laminated plate theory. The two formulations allow for any desired nonlinear isotropic or anisotropic material model as well as arbitrary large strains and deformations. The presented shell models can be used to analyze any arrangement and material behavior of the laminate layers. The FE solution is based on isogeometric analysis (IGA). Quadratic NURBS-based elements are used to ensure the smoothness required for the analysis of thin shells. The robustness and accuracy of the formulation is demonstrated by various numerical examples.

Keywords: Anisotropic composites, equivalent single layer shell theory, isogeometric analysis, laminated shell, Kirchhoff–Love theory, rotation-free shell

1 Introduction

Laminated composite shells are widely used in aerospace and automobile industries as well as other areas in civil, mechanical and manufacturing engineering due to their high stiffness-to-weight ratio. Further, one can find many applications in nano- and micro-electromechanical systems (Lyshevski, 2002), which can be best modeled by thin composite structures. The theoretical and numerical analysis of laminated composite shells has been the subject of extensive research in the last decades (for detailed surveys, see e.g. Reddy and Robbins, 1994; Yang et al., 2000; Carrera, 2002; Carrera and Brischetto, 2009; Zhang and Yang, 2009; Qatu et al., 2010; Kreja, 2011; Qatu et al., 2012). In particular, different theories and methodologies for the modeling and analysis of composite laminates are collected in the classic references of Ochoa and Reddy (1992), Carrera (2002) and Reddy (2004). In general, there are three different approaches to describe a composite laminate: (1) Equivalent single layer (ESL), (2) layer-wise (LW) and (3) continuum-based theories (Reddy, 1989). An equivalent single layer theory assumes a continuous strain distribution, which is usually considered to be linear, within the laminated layers of the shell. In contrast, in a layer-wise theory, piecewise continuous strain distributions are considered for each layer. In the third approach, a laminated shell is modeled as a 3D continuum with appropriate assumptions for the thickness.

¹corresponding author, email: sauer@aices.rwth-aachen.de

²This pdf is the personal version of an article whose final publication is available at <http://www.worldscientific.com/>

Regarding the material modeling, there are different micromechanical homogenization methods for composite materials (Li and Wang, 2008). For instance, Lin et al. (2016) examine different micromechanics methods, most of which are based on the Eshelby inclusion theory (Eshelby, 1957), to evaluate the effective moduli of soft Neo-Hookean composites. The Eshelby theory is later extended for the analysis of plates and shells. For example, Vel and Batra (1999, 2000, 2001) use the Eshelby-Stroh formalism (Eshelby et al., 1953; Stroh, 1958) to provide closed form solutions for anisotropic laminated plates in terms of infinite series. Furthermore, Aragh et al. (2012), Lei et al. (2013) and Thomas and Roy (2015) have used the Eshelby–Mori–Tanaka approach (Eshelby, 1957; Mori and Tanaka, 1973) for the structural analysis of carbon nanotube-reinforced plates and panels. The homogenization of the shell layers corresponds to thickness integration in shell theory, which is inherent to most shell theories and is performed either analytically or numerically.

In the last few years, various formulations are introduced for the the modeling of thin laminated composite shells based on isogeometric analysis, many of which follow the ESL approach. For instance, Bazilevs et al. (2011) use the bending strip method of Kiendl et al. (2010) to model composite rotor blades; however, they consider only a linear strain-stress relation, based on St. Venant–Kirchhoff material model. The formulation is later extended by Bazilevs et al. (2015); Deng et al. (2015) to predict damage in composites. Furthermore, Kapoor and Kapania (2012), Casanova (2013), Thai et al. (2014) and Thai et al. (2015) present isogeometric formulations for the analysis of composite plates based on first and higher order shear deformation theories. On the other hand, the LW approach is also investigated for the isogeometric analysis of laminated composites, in particular thin shells (Thai et al., 2013; Guo et al., 2014a,b; Guo and Ruess, 2015; Guo, 2016). Besides, 3D continuum shell formulations are also used for the modeling of composite materials in the framework of IGA (Hosseini et al., 2014, 2015).

In the current paper, the isogeometric finite shell element formulation of Duong et al. (2016) and Roohbakhshan and Sauer (2016) is extended to model thin composite shells. The presented model is based on ESL theory and it adds the following novelties to the existing literature on the computational modeling of thin laminated composite shells: (1) It allows any isotropic or anisotropic *nonlinear* constitution and yet (2) it does not need any *numerical integration* through the shell thickness. Furthermore, since the laminated composite shells are usually fiber-reinforced, the in-plane anisotropy is systematically considered in the computational model.

The next sections of this paper are organized as follows: Sec. 2 describes the theoretical framework including the rotation-free thin shell theory and composite shell models. Sec. 3 discusses the methodology of this work, i.e. NURBS-based FE solution. In Sec. 4, several numerical examples are presented to illustrate the capabilities of the introduced models. Sec. 5 concludes the paper.

2 Theory of composite shells

Equivalent single layer theories include the classical laminated plate theory (CLPT), the first order shear deformation theory (FSDT) and higher order shear deformation theory (HSDT) (Reddy, 2004). Here, we adopt the kinematics inherent to classical laminated plate theory, which is based on the Kirchhoff–Love hypothesis. Thus, it is assumed that the shell cross sections (1) remain straight, (2) do not elongate and (3) remain perpendicular to the shell mid-surface after deformation.

Beside the Kirchhoff–Love assumptions, the following assumptions are also considered: (1) The layers are perfectly bonded together. (2) Each layer is of uniform thickness. (3) The

material can have any desired nonlinear isotropic or anisotropic constitution. (4) The strains and deformations can be arbitrary large.

As shown in Fig. 1, we describe the laminated layers of a composite shell for two cases. In the general setup, the laminated layers can have different thickness and mechanical properties and they are not necessarily symmetric w.r.t. the shell mid-surface. As a specific case, one can suppose that the geometrical and material properties of laminates are symmetric w.r.t. the shell mid-surface. For both the cases, the boundaries of each layer are defined by the distance T_i measured from the mid-surface. Accordingly, the i^{th} layer is located between T_{i-1} and T_i , where $i = 1, \dots, n_1$. For the general case, n_1 is the total number of layers, numbered from the bottom to the top surface of the shell so that $T_0 = -T/2$ and $T_{n_1} = T/2$ (see Fig. 1.a). For the symmetric case, the total number of layers is $2n_1$ and the layer numbers are mirrored w.r.t. the mid-surface implying $T_0 = 0$ and $T_{n_1} = T/2$ (see Fig. 1.b).

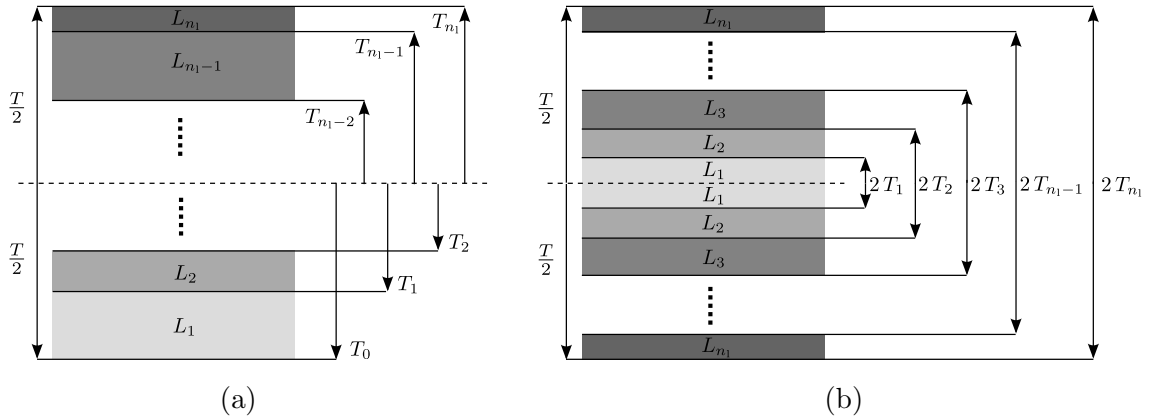


Figure 1: Coordinate system and layer numbering of a laminated shell: (a) General and (b) symmetric configurations.

2.1 Thin shell theory

Thin rotation-free shells are formulated based on classical shell theory, which roots in the Kirchhoff-Love hypothesis (Reddy, 2006); thus, the unknowns are only the displacement degrees of freedom. The kinematics and the governing equations of thin shells are summarized here. For a detailed description see e.g. Naghdi (1982), Steigmann (1999) and Sauer and Duong (2015). The presented theory is based on the differential geometry of curved surfaces (see e.g. Kreyszig, 1991); therefore, the formulations are described in a convective curvilinear coordinate system.

Note 2.1. Following the terminology of Duong et al. (2016) and Roohbakhshan and Sauer (2016), (1) the variables of three-dimensional continua are distinguished by a tilde. (2) The corresponding quantities of a shell layer \mathcal{S} , located at ξ within the shell thickness, are specified by an asterisk. (3) A hat is used to denote the quantities calculated at $\xi = 0$, i.e. $\hat{\bullet} = (\bullet^*)_{\xi=0}$. In general, such quantities can be defined for each shell layer and, on the shell mid-surface, they can be dimensionally linked to a counterpart in membrane theory (e.g. $a_{\alpha\beta} = \hat{g}_{\alpha\beta}$ or $\tau^{\alpha\beta} = T \hat{\tau}^{\alpha\beta}$) or there might be no corresponding quantity (e.g. for $\hat{\tau}_{,3}^{\alpha\beta}$) in membrane theory. (4) All the variables in the reference and current configurations are denoted by uppercase and lowercase letters, respectively.

2.1.1 Kinematics

In the current configuration, the shell mid-surface $\mathcal{S} = \hat{\mathcal{S}}$ can be described by the mapping

$$\mathbf{x} = \mathbf{x}(\xi^\alpha), \quad (\alpha = 1, 2), \quad (1)$$

where ξ^α are the convective coordinates defined in a parametric domain. According to this surface parameterization, the co-variant tangent vectors $\mathbf{a}_\alpha = \partial \mathbf{x} / \partial \xi^\alpha$ are obtained, which leads to the metric tensor with co-variant components $a_{\alpha\beta} = \mathbf{a}_\alpha \cdot \mathbf{a}_\beta$ and contra-variant components $[a^{\alpha\beta}] = [a_{\alpha\beta}]^{-1}$. Then, the contra-variant tangent vectors can be obtained as $\mathbf{a}^\alpha = a^{\alpha\beta} \mathbf{a}_\beta$. The current surface area is $da = J_a d\xi^1 d\xi^2$, where $J_a := \sqrt{a_{\alpha\beta}}$ is the surface Jacobian determinant. Having the co-variant tangents at hand, the surface normals are defined as $\mathbf{n} = (\mathbf{a}_1 \times \mathbf{a}_2) / J_a$. Then, the co-variant components of the curvature tensor are $b_{\alpha\beta} = \mathbf{n} \cdot \mathbf{a}_{\alpha,\beta}$, where $\mathbf{a}_{\alpha,\beta} := \partial \mathbf{a}_\alpha / \partial \xi^\beta$ is the parametric derivative of \mathbf{a}_α . The convective bases $\{\mathbf{a}_1, \mathbf{a}_2, \mathbf{n}\}$ and $\{\mathbf{a}^1, \mathbf{a}^2, \mathbf{n}\}$ can then be used to decompose any vector or tensor into in-plane and out-of-plane components. For instance, the usual identity tensor $\mathbf{1} \in \mathbb{R}^3$ is decomposed as

$$\mathbf{1} = \mathbf{i} + \mathbf{n} \otimes \mathbf{n}, \quad (2)$$

where

$$\mathbf{i} = a^{\alpha\beta} \mathbf{a}_\alpha \otimes \mathbf{a}_\beta = \mathbf{a}_\alpha \otimes \mathbf{a}^\alpha = \mathbf{a}^\alpha \otimes \mathbf{a}_\alpha \quad (3)$$

is the surface identity tensor. Similarly, corresponding quantities can be defined on the reference configuration \mathcal{S}_0 (see [Sauer et al., 2014](#); [Sauer and Duong, 2015](#), for more details).

For thin shells, the introduced description of the mid-surface can be extended to any shell layer $\hat{\mathcal{S}}^*$ located at $\xi \in [-T/2, T/2]$, where T is the shell thickness and ξ is an out-of-plane coordinate defined in the normal direction. Accordingly, any material point $\tilde{\mathbf{x}}$ in the 3D continuum of the shell is related to a corresponding point on the mid-surface as

$$\tilde{\mathbf{x}} = \mathbf{x} + \xi \mathbf{n}. \quad (4)$$

Such layer-wise kinematical description is required for the integration/projection process ([Duong et al., 2016](#)). Furthermore, it can be shown that the co-variant components of the metric tensor on the shell layer $\hat{\mathcal{S}}^*$ are

$$g_{\alpha\beta} = a_{\alpha\beta} - 2\xi b_{\alpha\beta} \quad (5)$$

and the corresponding contra-variant components are $[g^{\alpha\beta}] = [g_{\alpha\beta}]^{-1}$ ([Roohbakhshan and Sauer, 2016](#)). To describe the deformation and stress-strain relation, our formulation uses the right Cauchy–Green deformation tensor, the Green–Lagrange strain tensor and the bending strain tensor. The right Cauchy–Green deformation tensors on the mid-surface and the shell layer $\hat{\mathcal{S}}^*$ are, respectively

$$\begin{aligned} \mathbf{C} &= a_{\alpha\beta} \mathbf{A}^\alpha \otimes \mathbf{A}^\beta, \\ \hat{\mathbf{C}}^* &= g_{\alpha\beta} \mathbf{G}^\alpha \otimes \mathbf{G}^\beta. \end{aligned} \quad (6)$$

The corresponding Green–Lagrange strain tensors are defined as

$$\begin{aligned} \mathbf{E} &:= \frac{1}{2} (\mathbf{C} - \mathbf{I}) = E_{\alpha\beta} \mathbf{A}^\alpha \otimes \mathbf{A}^\beta, \\ \hat{\mathbf{E}}^* &:= \frac{1}{2} (\hat{\mathbf{C}}^* - \hat{\mathbf{I}}^*) = \hat{E}_{\alpha\beta}^* \mathbf{G}^\alpha \otimes \mathbf{G}^\beta, \end{aligned} \quad (7)$$

where \mathbf{I} and $\hat{\mathbf{I}}^*$ are the surface identity tensors for \mathcal{S}_0 and $\hat{\mathcal{S}}_0^*$ in the reference configuration,

$$E_{\alpha\beta} = \frac{1}{2} (a_{\alpha\beta} - A_{\alpha\beta}) \quad (8)$$

are the co-variant components of the Green–Lagrange strain on the mid-surface \mathcal{S} and

$$\dot{E}_{\alpha\beta}^* = \frac{1}{2} (g_{\alpha\beta} - G_{\alpha\beta}) \quad (9)$$

are the corresponding components on the shell layer $\dot{\mathcal{S}}^*$. Likewise to \mathbf{E} , the bending strain tensor is defined as

$$\mathbf{K} := K_{\alpha\beta} \mathbf{A}^\alpha \otimes \mathbf{A}^\beta, \quad (10)$$

with

$$K_{\alpha\beta} = b_{\alpha\beta} - B_{\alpha\beta}. \quad (11)$$

The variation of the introduced kinematical quantities can be found in [Sauer and Duong \(2015\)](#), [Duong et al. \(2016\)](#) and [Roohbakhshan and Sauer \(2016\)](#).

2.1.2 Governing equation

Considering the balance of linear momentum and mass conservation, the strong form of the governing equation is ([Sauer and Duong, 2015](#))

$$\mathbf{T}_{;\alpha}^\alpha + \mathbf{f} = \rho \dot{\mathbf{v}} \quad \forall \mathbf{x} \in \mathcal{S}, \quad (12)$$

where \mathbf{T}^α is the traction vector defined on the face normal to \mathbf{a}^α , $\mathbf{f} = f^\alpha \mathbf{a}_\alpha + p \mathbf{n}$ is the prescribed body force on \mathcal{S} , ρ is the mass per current surface area and $\dot{\mathbf{v}}$ is the material acceleration. In general, on a face normal to $\boldsymbol{\nu} = \nu_\alpha \mathbf{a}^\alpha$, the sectional forces are collected in the stress tensor

$$\boldsymbol{\sigma} := N^{\alpha\beta} \mathbf{a}_\alpha \otimes \mathbf{a}_\beta + S^\alpha \mathbf{a}_\alpha \otimes \mathbf{n} \quad (13)$$

and the distributed section moments are collected in the moment tensor

$$\boldsymbol{\mu} := -M^{\alpha\beta} \mathbf{a}_\alpha \otimes \mathbf{a}_\beta \quad (14)$$

such that the traction and the distributed moment vectors are given by Cauchy's theorem as

$$\begin{aligned} \mathbf{T} &:= \boldsymbol{\sigma}^T \boldsymbol{\nu}, \\ \mathbf{M} &:= \boldsymbol{\mu}^T \boldsymbol{\nu}. \end{aligned} \quad (15)$$

Here, $N^{\alpha\beta}$, S^α and $M^{\alpha\beta}$ are the distributed sectional force and moment components (see [Sauer and Duong \(2015\)](#) for details). Furthermore, it can be shown that ([Sauer and Duong, 2015](#))

$$\begin{aligned} \sigma^{\alpha\beta} &= N^{\alpha\beta} - b_\gamma^\beta M^{\gamma\alpha}, \\ S^\alpha &= M_{;\beta}^{\beta\alpha}, \end{aligned} \quad (16)$$

where $\sigma^{\alpha\beta}$ and $M^{\alpha\beta}$ follow from constitution.

Introducing $\tau^{\alpha\beta} = J \sigma^{\alpha\beta}$ and $M_0^{\alpha\beta} = J M^{\alpha\beta}$, for any admissible variation $\delta \mathbf{x} \in \mathcal{V}$, the weak form of Eq. (12) is derived as ([Sauer and Duong, 2015](#))

$$G_{\text{in}} + G_{\text{int}} - G_{\text{ext}} = 0 \quad \forall \delta \mathbf{x} \in \mathcal{V}, \quad (17)$$

where we have defined the inertial, internal and external virtual work contributions due to variation $\delta \mathbf{x}$, respectively as

$$\begin{aligned} G_{\text{in}} &= \int_{\mathcal{S}_0} \delta \mathbf{x} \cdot \rho_0 \dot{\mathbf{v}} \, dA, \\ G_{\text{int}} &= \int_{\mathcal{S}_0} \frac{1}{2} \delta a_{\alpha\beta} \tau^{\alpha\beta} \, dA + \int_{\mathcal{S}_0} \delta b_{\alpha\beta} M_0^{\alpha\beta} \, dA, \\ G_{\text{ext}} &= \int_{\mathcal{S}} \delta \mathbf{x} \cdot \mathbf{f} \, da + \int_{\partial_t \mathcal{S}} \delta \mathbf{x} \cdot \mathbf{t} \, ds + \int_{\partial_m \mathcal{S}} \delta \mathbf{n} \cdot m_\tau \boldsymbol{\nu} \, ds + [\delta \mathbf{x} \cdot m_\nu \mathbf{n}]. \end{aligned} \quad (18)$$

Here, \mathbf{t} , m_τ and m_ν are distributed forces and moments prescribed on the boundary. It should be noted that ρ_0 , $\tau^{\alpha\beta}$ and $M_0^{\alpha\beta}$ are surface quantities resulting from thickness integration, as addressed in Sec. 2.2.

2.1.3 Linearized weak form

The weak form (17) is highly nonlinear, and needs to be linearized w.r.t. the metric and curvature tensors, in order to be solved by the Newton–Raphson method (see Sec. 3.4). Following Sauer and Duong (2015) and Duong et al. (2016), the linearization in the absence of inertial and non-constant external forces is

$$\begin{aligned} \Delta G_{\text{int}} &= \int_{\mathcal{S}_0} \frac{1}{2} \delta a_{\alpha\beta} \left(c^{\alpha\beta\gamma\delta} \frac{1}{2} \Delta a_{\gamma\delta} + d^{\alpha\beta\gamma\delta} \Delta b_{\gamma\delta} \right) dA \\ &+ \int_{\mathcal{S}_0} \delta b_{\alpha\beta} \left(e^{\alpha\beta\gamma\delta} \frac{1}{2} \Delta a_{\gamma\delta} + f^{\alpha\beta\gamma\delta} \Delta b_{\gamma\delta} \right) dA \\ &+ \int_{\mathcal{S}_0} \left(\tau^{\alpha\beta} \frac{1}{2} \Delta \delta a_{\alpha\beta} + M_0^{\alpha\beta} \Delta \delta b_{\alpha\beta} \right) dA, \end{aligned} \quad (19)$$

where

$$\begin{aligned} c^{\alpha\beta\gamma\delta} &:= 2 \frac{\partial \tau^{\alpha\beta}}{\partial a_{\gamma\delta}}, & d^{\alpha\beta\gamma\delta} &:= \frac{\partial \tau^{\alpha\beta}}{\partial b_{\gamma\delta}}, \\ e^{\alpha\beta\gamma\delta} &:= 2 \frac{\partial M_0^{\alpha\beta}}{\partial a_{\gamma\delta}}, & f^{\alpha\beta\gamma\delta} &:= \frac{\partial M_0^{\alpha\beta}}{\partial b_{\gamma\delta}} \end{aligned} \quad (20)$$

are the material tangents.

2.2 Thin composite shell models

In Roohbakhshan and Sauer (2016), three different models – namely the *numerically-projected shell model*, *analytically-projected shell model* and *directly-decoupled shell model* – are introduced to formulate the constitutive laws, stress and bending moment resultants and their corresponding stiffness tangents. Here, those three shell models are extended to laminated composite shells.

2.2.1 Numerically-projected shell model

The numerically-projected shell model is the most general formulation that can be used for both the asymmetric and symmetric composite shells; however, it generally requires numerical integration through the shell thickness. The stress and bending moment resultants thus are (Roohbakhshan and Sauer, 2016)

$$\begin{aligned} \tau^{\alpha\beta} &= \sum_{i=1}^{n_1} \int_{T_{i-1}}^{T_i} \tilde{\tau}_i^{\alpha\beta} d\xi, \\ M_0^{\alpha\beta} &= - \sum_{i=1}^{n_1} \int_{T_{i-1}}^{T_i} \xi \tilde{\tau}_i^{\alpha\beta} d\xi. \end{aligned} \quad (21)$$

where

$$\tilde{\tau}_i^{\alpha\beta} := 2 \frac{\partial \tilde{W}_i(g_{\alpha\beta})}{\partial g_{\alpha\beta}} \quad (22)$$

is the in-plane Kirchhoff stress on a shell layer within the i^{th} laminate and $\tilde{W}_i(g_{\alpha\beta})$ is the strain energy density function of the same laminate layer. In the same fashion, the stiffness tangents are

$$\begin{aligned} c^{\alpha\beta\gamma\delta} &= \sum_{i=1}^{n_1} \int_{T_{i-1}}^{T_i} \tilde{c}_i^{\alpha\beta\gamma\delta} d\xi, \\ d^{\alpha\beta\gamma\delta} &= e^{\alpha\beta\gamma\delta} = - \sum_{i=1}^{n_1} \int_{T_{i-1}}^{T_i} \xi \tilde{c}_i^{\alpha\beta\gamma\delta} d\xi, \\ f^{\alpha\beta\gamma\delta} &= \sum_{i=1}^{n_1} \int_{T_{i-1}}^{T_i} \xi^2 \tilde{c}_i^{\alpha\beta\gamma\delta} d\xi, \end{aligned} \quad (23)$$

where

$$\tilde{c}_i^{\alpha\beta\gamma\delta} := 2 \frac{\partial \tilde{\tau}_i^{\alpha\beta}}{\partial g_{\gamma\delta}} = 4 \frac{\partial^2 \tilde{W}_i(g_{\alpha\beta})}{\partial g_{\alpha\beta} \partial g_{\gamma\delta}}. \quad (24)$$

2.2.2 Analytically-projected shell model

Following [Roohbakhshan and Sauer \(2016\)](#), one can use a first-order Taylor expansion of $\tilde{\tau}_i^{\alpha\beta}$ about $\xi = 0$ to approximate the stress and bending moment resultants given by Eq. (21). In this approach, one can then analytically evaluate the integrals of Eq. (21) without any need for numerical integration. For all the laminates through the shell thickness, the stress is thus approximated as

$$\tilde{\tau}_i^{\alpha\beta} = \hat{\tau}_i^{\alpha\beta} + \xi \hat{\tau}_{i,3}^{\alpha\beta}, \quad (25)$$

where we have defined

$$\begin{aligned} \hat{\tau}_i^{\alpha\beta} &:= \left(\tilde{\tau}_i^{\alpha\beta} \right)_{\xi=0}, \\ \hat{\tau}_{i,3}^{\alpha\beta} &:= \left(\frac{\partial \tilde{\tau}_i^{\alpha\beta}}{\partial \xi} \right)_{\xi=0}. \end{aligned} \quad (26)$$

2.2.2.1 General setup

Plugging Eq. (25) into Eq. (21) and integrating analytically, we obtain (see Fig. 1.a)

$$\begin{aligned} \tau^{\alpha\beta} &= \sum_{i=1}^{n_1} \left[(T_i - T_{i-1}) \hat{\tau}_i^{\alpha\beta} + \frac{1}{2} (T_i^2 - T_{i-1}^2) \hat{\tau}_{i,3}^{\alpha\beta} \right], \\ M_0^{\alpha\beta} &= \sum_{i=1}^{n_1} \left[\frac{1}{2} (T_{i-1}^2 - T_i^2) \hat{\tau}_i^{\alpha\beta} + \frac{1}{3} (T_{i-1}^3 - T_i^3) \hat{\tau}_{i,3}^{\alpha\beta} \right]. \end{aligned} \quad (27)$$

The corresponding stiffness tangents are

$$\begin{aligned} c^{\alpha\beta\gamma\delta} &= \sum_{i=1}^{n_1} \left[(T_i - T_{i-1}) \hat{c}_i^{\alpha\beta\gamma\delta} + \frac{1}{2} (T_i^2 - T_{i-1}^2) \hat{c}_{i,3}^{\alpha\beta\gamma\delta} \right], \\ d^{\alpha\beta\gamma\delta} &= \sum_{i=1}^{n_1} \left[(T_i - T_{i-1}) \hat{d}_i^{\alpha\beta\gamma\delta} + \frac{1}{2} (T_i^2 - T_{i-1}^2) \hat{d}_{i,3}^{\alpha\beta\gamma\delta} \right], \\ e^{\alpha\beta\gamma\delta} &= \sum_{i=1}^{n_1} \left[\frac{1}{2} (T_{i-1}^2 - T_i^2) \hat{c}_i^{\alpha\beta\gamma\delta} + \frac{1}{3} (T_{i-1}^3 - T_i^3) \hat{c}_{i,3}^{\alpha\beta\gamma\delta} \right], \\ f^{\alpha\beta\gamma\delta} &= \sum_{i=1}^{n_1} \left[\frac{1}{2} (T_{i-1}^2 - T_i^2) \hat{d}_i^{\alpha\beta\gamma\delta} + \frac{1}{3} (T_{i-1}^3 - T_i^3) \hat{d}_{i,3}^{\alpha\beta\gamma\delta} \right], \end{aligned} \quad (28)$$

for which we have introduced

$$\begin{aligned}\hat{c}_i^{\alpha\beta\gamma\delta} &= 2 \frac{\partial \hat{\tau}_i^{\alpha\beta}}{\partial a_{\gamma\delta}}, & \hat{d}_i^{\alpha\beta\gamma\delta} &= \frac{\partial \hat{\tau}_i^{\alpha\beta}}{\partial b_{\gamma\delta}}, \\ \hat{c}_{i,3}^{\alpha\beta\gamma\delta} &= 2 \frac{\partial \hat{\tau}_{i,3}^{\alpha\beta}}{\partial a_{\gamma\delta}}, & \hat{d}_{i,3}^{\alpha\beta\gamma\delta} &= \frac{\partial \hat{\tau}_{i,3}^{\alpha\beta}}{\partial b_{\gamma\delta}}.\end{aligned}\tag{29}$$

2.2.2.2 Symmetric setup

If the laminated layers are distributed symmetrically w.r.t. the shell mid-surface, Eq. (27) can be reduced to

$$\begin{aligned}\tau^{\alpha\beta} &= 2 \sum_{i=1}^{n_1} (T_i - T_{i-1}) \hat{\tau}_i^{\alpha\beta}, \\ M_0^{\alpha\beta} &= -\frac{2}{3} \sum_{i=1}^{n_1} (T_i^3 - T_{i-1}^3) \hat{\tau}_{i,3}^{\alpha\beta},\end{aligned}\tag{30}$$

where the layers are numbered according to Fig. 1.b. From Eq. (30), the stiffness tangents are derived as

$$\begin{aligned}e^{\alpha\beta\gamma\delta} &= 2 \sum_{i=1}^{n_1} (T_i - T_{i-1}) \hat{c}_i^{\alpha\beta\gamma\delta}, & d^{\alpha\beta\gamma\delta} &= 2 \sum_{i=1}^{n_1} (T_i - T_{i-1}) \hat{d}_i^{\alpha\beta\gamma\delta}, \\ e^{\alpha\beta\gamma\delta} &= -\frac{2}{3} \sum_{i=1}^{n_1} (T_i^3 - T_{i-1}^3) \hat{c}_{i,3}^{\alpha\beta\gamma\delta}, & f^{\alpha\beta\gamma\delta} &= -\frac{2}{3} \sum_{i=1}^{n_1} (T_i^3 - T_{i-1}^3) \hat{d}_{i,3}^{\alpha\beta\gamma\delta}.\end{aligned}\tag{31}$$

Remark 2.2. In the formulations presented so far, it is assumed that the shell is *fully-stressed*, i.e. all the layers through the shell thickness contribute to the strain energy density function and the corresponding stress and bending moment resultants. However, as discussed by [Roohbakhshan and Sauer \(2016\)](#), depending on the constitution and application, the shell might only be *partially-stressed*, i.e. within each laminate layer, only a portion of shell $[T_{i1}, T_{i2}] \subset [T_{i-1}, T_i]$ might be active. Such a scenario happens e.g. for concrete, which bears only compression, or collagen fibers, which support only tension. This implies that

$$\begin{aligned}\tau^{\alpha\beta} &= \sum_{i=1}^{n_1} \int_{T_{i1}}^{T_{i2}} \tilde{\tau}_i^{\alpha\beta} d\xi, \\ M_0^{\alpha\beta} &= -\sum_{i=1}^{n_1} \int_{T_{i1}}^{T_{i2}} \xi \tilde{\tau}_i^{\alpha\beta} d\xi\end{aligned}\tag{32}$$

for the numerically-projected approach and

$$\begin{aligned}\tau^{\alpha\beta} &= \sum_{i=1}^{n_1} \left[(T_{i2} - T_{i1}) \hat{\tau}_i^{\alpha\beta} + \frac{1}{2} (T_{i2}^2 - T_{i1}^2) \hat{\tau}_{i,3}^{\alpha\beta} \right], \\ M_0^{\alpha\beta} &= \sum_{i=1}^{n_1} \left[\frac{1}{2} (T_{i1}^2 - T_{i2}^2) \hat{\tau}_i^{\alpha\beta} + \frac{1}{3} (T_{i1}^3 - T_{i2}^3) \hat{\tau}_{i,3}^{\alpha\beta} \right]\end{aligned}\tag{33}$$

for the analytically-projected approach, where T_{i1} and T_{i2} need to be determined specifically for each problem.

2.2.3 Directly-decoupled shell model

The directly-decoupled shell model is based on the idea that the stored energy of a thin shell, whose material is symmetric w.r.t. the shell mid-surface, can be fully decoupled into membrane and bending parts (Roohbakhshan and Sauer, 2016). Hence, the directly-decoupled approach only works for symmetric laminated shells. Accordingly, the stored energy W is decoupled as

$$W(a_{\alpha\beta}, b_{\alpha\beta}) = W_M(a_{\alpha\beta}) + W_B(b_{\alpha\beta}) , \quad (34)$$

where the membrane part W_M can be obtained e.g. by the projection method of Roohbakhshan et al. (2016), which results in

$$W_M(a_{\alpha\beta}) = \sum_{i=1}^{n_1} (T_i - T_{i-1}) \hat{W}_i(a_{\alpha\beta}) , \quad (35)$$

where

$$\hat{W}_i(a_{\alpha\beta}) := \left[\tilde{W}_i(g_{\alpha\beta}) \right]_{\xi=0} \quad (36)$$

is the constitutive law of the i^{th} laminate layer formulated in terms of the mid-surface metric tensor $a_{\alpha\beta}$. The bending part is then

$$W_B(b_{\alpha\beta}) = \frac{1}{24} \sum_{i=1}^{n_1} (T_i^3 - T_{i-1}^3) \hat{c}_{0i}^{\alpha\beta\gamma\delta} K_{\alpha\beta} K_{\gamma\delta} , \quad (37)$$

where

$$\hat{c}_{0i}^{\alpha\beta\gamma\delta} := \left(\hat{c}_i^{\alpha\beta\gamma\delta} \right)_{\mathcal{S}_0} \quad (38)$$

are the components of the membrane elasticity tensor prior to deformation and

$$\hat{c}_i^{\alpha\beta\gamma\delta} := 4 \frac{\partial^2 \hat{W}_i(a_{\alpha\beta})}{\partial a_{\alpha\beta} \partial a_{\gamma\delta}} . \quad (39)$$

Thus, the stress and bending moment resultants are

$$\begin{aligned} \tau^{\alpha\beta} &:= 2 \frac{\partial W_M(a_{\alpha\beta})}{\partial a_{\alpha\beta}} = 2 \sum_{i=1}^{n_1} (T_i - T_{i-1}) \hat{\tau}_i^{\alpha\beta} , \\ M_0^{\alpha\beta} &:= \frac{\partial W_B(b_{\alpha\beta})}{\partial b_{\alpha\beta}} = \frac{2}{3} \sum_{i=1}^{n_1} (T_i^3 - T_{i-1}^3) \hat{c}_{0i}^{\alpha\beta\gamma\delta} K_{\gamma\delta} , \end{aligned} \quad (40)$$

with

$$\hat{\tau}_i^{\alpha\beta} := 2 \frac{\partial \hat{W}_i(a_{\alpha\beta})}{\partial a_{\alpha\beta}} . \quad (41)$$

The corresponding stiffness tangents are

$$\begin{aligned} c^{\alpha\beta\gamma\delta} &= 2 \sum_{i=1}^{n_1} (T_i - T_{i-1}) \hat{c}_i^{\alpha\beta\gamma\delta} , \\ f^{\alpha\beta\gamma\delta} &= \frac{2}{3} \sum_{i=1}^{n_1} (T_i^3 - T_{i-1}^3) \hat{c}_{0i}^{\alpha\beta\gamma\delta} \end{aligned} \quad (42)$$

and $d^{\alpha\beta\gamma\delta} = e^{\alpha\beta\gamma\delta} = 0$, which illustrates the decoupling.

3 FE Solution

The finite element solution is based on the IGA concept (Hughes et al., 2005), which uses non-uniform rational B-spline (NURBS) functions for both the geometrical representation and discretization of the weak form (17). The main advantage of NURBS-based finite elements is the high smoothness in the representation of geometry and solution, which satisfies the C^1 -continuity required for the modeling of thin rotation-free shells based on the Kirchhoff–Love hypothesis (Kiendl et al., 2009). Furthermore, quadratic and higher order NURBS-based FE discretizations help to remove membrane locking. This section summarizes the main steps of the FE solution, i.e. isogeometric discretization, FE approximation and discretized weak form. Further details of the FE implementation can be found in Duong et al. (2016).

3.1 Isogeometric discretization

A comprehensive description of NURBS and B-splines is outside the scope of this paper and further conceptual, theoretical and mathematical details can be found in the classical references for IGA (e.g. Hughes et al., 2005; Cottrell et al., 2009). In general, a NURBS-based surface, which is an extension of a B-spline surface, is described by a mapping from a two dimensional parametric domain. The mapping is determined by the desired polynomial order p and q for each dimension, a set of control points $\mathbf{P} = \{\mathbf{P}_A\}_{A=1}^{n_{cp}}$ that define the shape, and two knot vectors $\Xi = \{\xi_1, \xi_2, \dots, \xi_{n+p+1}\}$ and $\mathcal{H} = \{\eta_1, \eta_2, \dots, \eta_{m+q+1}\}$. Here, $n_{cp} = n \times m$ is the total number of control points of the patch with m and n to be the number of control points in the directions ξ and η , respectively. Besides, for the numbering of control points, we need to define a mapping $A = A(i, j)$ based on the grid of control points, where $i = 1, \dots, n$ and $j = 1, \dots, m$. The NURBS surface is constructed from the rational basis functions

$$R_A^{p,q}(\xi, \eta) = \frac{w_A \hat{N}_i^p(\xi) \hat{N}_j^q(\eta)}{W(\xi, \eta)}, \quad (43)$$

where w_A are the weights associated to the control points and $\hat{N}_i^p(\xi)$ and $\hat{N}_j^q(\eta)$ are the B-spline basis functions in each dimension and the weighting function is

$$W(\xi, \eta) = \sum_{k=1}^n \sum_{l=1}^m w_B \hat{N}_k^p(\xi) \hat{N}_l^q(\eta), \quad (44)$$

with $B = A(k, l)$. In matrix form, Eq. (43) can be written as

$$\mathbf{R}(\xi, \eta) = \frac{\mathbf{W} \hat{\mathbf{N}}(\xi, \eta)}{W(\xi, \eta)}, \quad (45)$$

where $\mathbf{R}(\xi, \eta) := \{R_A^{p,q}(\xi, \eta)\}_{A=1}^{n_{cp}}$, $\hat{\mathbf{N}}(\xi, \eta) := \{\hat{N}_i^p(\xi) \hat{N}_j^q(\eta)\}_{A=1}^{n_{cp}}$ and \mathbf{W} is a diagonal matrix containing the weights of the control points. Then, the shell mid-surface is discretized by NURBS as

$$\mathbf{x}(\xi, \eta) = \sum_{i=1}^{n_{cp}} R_A^{p,q}(\xi, \eta) \mathbf{P}_A = \mathbf{P}^T \mathbf{R}(\xi, \eta), \quad \xi \in [\xi_1, \xi_{n+p+1}], \quad \eta \in [\eta_1, \eta_{m+q+1}], \quad (46)$$

where $\mathbf{P} := \{\mathbf{P}_A\}_{A=1}^{n_{cp}}$.

Furthermore, with the help of the Bézier extraction operator (Borden et al., 2011), the global parametric domains Ξ and \mathcal{H} are changed to the domain of the Bézier elements. Then the shape

functions are implemented as a classical FEM. Thus, the rational shape function of an element Ω^e is defined as

$$\mathbf{R}^e(\xi, \eta) = \frac{\mathbf{W}^e \mathbf{C}^e \mathbf{B}^e}{W(\xi, \eta)}, \quad \xi, \eta \in [-1, 1], \quad (47)$$

where $\mathbf{R}^e(\xi, \eta) = \{R_A^e(\xi, \eta)\}_{A=1}^{n_{\text{cp}}^e}$ is the set of the rational shape functions, n_{cp}^e is the number of control points per element, \mathbf{W}^e is the corresponding diagonal matrix of the element, \mathbf{B}^e collects the Bernstein polynomials of the element and $\mathbf{C}^e = \mathbf{C}_\xi^e \otimes \mathbf{C}_\eta^e$ is the localized Bézier extraction operator. To construct the classic finite element setup, for the A^{th} control point (=node), the corresponding shape function in element Ω^e is set to $N_A(\xi, \eta) = R_A^e(\xi, \eta)$, where R_A^e is given by Eq. (47).

3.2 FE approximation

Having the finite element shape functions, any point in the reference element Ω_0^e and deformed element Ω^e are obtained by the interpolation

$$\mathbf{X} = \mathbf{N} \mathbf{X}_e, \quad \mathbf{x} = \mathbf{N} \mathbf{x}_e, \quad (48)$$

where \mathbf{X}_e and \mathbf{x}_e are the positions of the control points in the reference and current configurations, respectively, and $\mathbf{N}(\boldsymbol{\xi}) := [N_1 \mathbf{1}, N_2 \mathbf{1}, \dots, N_{n_{\text{cp}}} \mathbf{1}]$ is defined based on the NURBS shape functions of Eq. (47). Having interpolation (48), the surface objects, such as \mathbf{a}_α , $\mathbf{a}_{\alpha,\beta}$ and $\mathbf{a}_{\alpha;\beta}$, are interpolated in the same fashion, e.g. $\mathbf{a}_\alpha = \mathbf{N}_{,\alpha} \mathbf{x}_e$, where we have defined $\mathbf{N}_{,\alpha}(\boldsymbol{\xi}) := [N_{1,\alpha} \mathbf{1}, N_{2,\alpha} \mathbf{1}, \dots, N_{n_{\text{cp}},\alpha} \mathbf{1}]$ and $N_{A,\alpha} = \partial N_A / \partial \xi^\alpha$. Considering a Bubnov–Galerkin formulation, the variation $\delta \mathbf{x}$ is also approximated in the same way as the deformation, i.e. $\delta \mathbf{x} = \mathbf{N} \delta \mathbf{x}_e$ (see Duong et al., 2016, for more details).

3.3 Discretized weak form

Based on the introduced FE setting, the shell weak form (17) can be discretized, i.e. the surface integration (e.g. Eq. (18)) is carried out over the element domains Ω^e and then summed over all the finite elements as

$$\sum_{e=1}^{n_{\text{el}}} (G_{\text{in}}^e + G_{\text{int}}^e - G_{\text{ext}}^e) = 0 \quad \forall \delta \mathbf{x}_e \in \mathcal{V}, \quad (49)$$

where

$$\begin{aligned} G_{\text{in}}^e &= \delta \mathbf{x}_e^T \mathbf{f}_{\text{in}}^e, \\ G_{\text{int}}^e &= \delta \mathbf{x}_e^T (\mathbf{f}_{\text{int}}^e), \\ G_{\text{ext}}^e &= \delta \mathbf{x}_e^T (\mathbf{f}_{\text{ext}}^e) \end{aligned} \quad (50)$$

and force vectors \mathbf{f}_{in}^e , $\mathbf{f}_{\text{int}}^e$ and $\mathbf{f}_{\text{ext}}^e$ are given by (Duong et al., 2016). Eqs. (49) and (50) result in the nonlinear system of equations

$$\mathbf{f} = \mathbf{A} \begin{matrix} n_{\text{el}} \\ \mathbf{f}_{\text{in}}^e + \mathbf{f}_{\text{int}}^e - \mathbf{f}_{\text{ext}}^e \end{matrix} = \mathbf{0}, \quad (51)$$

which is constructed by the assembly of the element force vectors.

3.4 Newton–Raphson iteration

As $\mathbf{f} = \mathbf{f}(\mathbf{x})$ is highly non-linear, it needs to be solved iteratively, e.g. by the Newton–Raphson method. This requires linearization of \mathbf{f} w.r.t. \mathbf{x} as

$$\Delta \mathbf{f} = \mathbf{k} \Delta \mathbf{x} , \quad (52)$$

where

$$\mathbf{k} := \mathbf{A}_{e=1}^{n_{el}} (\mathbf{k}_{\text{int}}^e - \mathbf{k}_{\text{ext}}^e) , \quad (53)$$

is the global stiffness matrix, built by the assembly of element stiffness matrices

$$\mathbf{k}_{\text{int}}^e := \frac{\partial \mathbf{f}_{\text{int}}^e}{\partial \mathbf{x}_e} , \quad \mathbf{k}_{\text{ext}}^e := \frac{\partial \mathbf{f}_{\text{ext}}^e}{\partial \mathbf{x}_e} , \quad (54)$$

which can be found in detail in [Duong et al. \(2016\)](#).

3.5 Numerical integration

Two kinds of numerical integration are needed for the presented formulation. First and foremost, the evaluation of weak form (18) requires numerical integration, which is performed with standard Gaussian quadrature over a master domain $\xi^\alpha \in [-1, 1]$, $\alpha = 1, 2$, like in classic FEA. Second, if the numerically-projected shell model of Sec. 2.2.1 is used, the stress and bending moment resultants and their corresponding tangents, i.e. Eqs. (21) and (23), are evaluated by numerical integration. Similarly, the integration is carried out over a master domain $\theta \in [-1, 1]$. For laminated composite shells, the change of integration interval needs to be taken into account. For instance, the stress resultant is numerically approximated as

$$\begin{aligned} \tau^{\alpha\beta}(\mathbf{x}) &= \sum_{i=1}^{n_l} \int_{T_{i-1}}^{T_i} \tilde{\tau}_i^{\alpha\beta}(\mathbf{x}, \xi) d\xi \\ &= \sum_{i=1}^{n_l} \frac{T_i - T_{i-1}}{2} \int_{-1}^{+1} \tilde{\tau}_i^{\alpha\beta}[\mathbf{x}, f_i(\theta)] d\theta \\ &\approx \sum_{i=1}^{n_l} \frac{T_i - T_{i-1}}{2} \sum_{j=1}^{n_{gp}} w_j \tilde{\tau}_i^{\alpha\beta}[\mathbf{x}, f_i(\theta_j)] , \end{aligned} \quad (55)$$

where

$$f_i(\theta) := \frac{1}{2} [T_i + T_{i-1} + (T_i - T_{i-1}) \theta] \quad (56)$$

and n_{gp} , w_j and θ_j are the total number, weight and position of Gaussian quadrature points in the master domain θ , respectively.

4 Numerical examples

In this section, three different numerical examples are investigated to show the performance of the proposed formulation. For each laminate configuration (see Fig. 1), an example is presented. The *analytically-projected* (AP) and *directly-decoupled* (DD) shell models, which do not need numerical integration through the shell thickness, are compared with the *numerically-projected*

(NP) shell model as the reference solution. The first example is devoted to a symmetric laminate configuration. The second example evaluates a general laminate configuration, where the laminate layers have arbitrary geometrical and material properties. Finally, the last example simulates the pressurization of a laminated composite tube.

For all the examples, an incompressible anisotropic 3D Mooney–Rivlin material model with two families of fibers is considered as

$$\tilde{W}(\tilde{I}_1, \tilde{J}) = \frac{\tilde{c}_1}{2}(\tilde{I}_1 - 3) + \frac{\tilde{c}_2}{2}(\tilde{I}_2 - 3) + \sum_{j=1}^{n_f} \tilde{c}_{3j}(\tilde{I}_4^j - 1)^2 + \tilde{p}\tilde{g}, \quad (57)$$

where \tilde{I}_1 , \tilde{I}_2 and \tilde{J} are the first, second and third invariants of the right Cauchy–Green deformation tensor $\tilde{\mathbf{C}}$, respectively, $\tilde{g} := \tilde{J} - 1$ is the incompressibility constraint and \tilde{p} is the corresponding Lagrange multiplier to impose the constraint, which can be eliminated analytically (see [Roohbakhshan and Sauer, 2016](#), for details). Further, \tilde{I}_4^j ($j = 1, \dots, n_f$) are the invariants of the structural tensor of the fibers $\tilde{\mathbf{M}}_j := \tilde{\mathbf{L}}_j \otimes \tilde{\mathbf{L}}_j$, where $\tilde{\mathbf{L}}_j$ is the principal direction of the j^{th} family of fibers.

Here, for all the laminate layers, the number of families of fibers is $n_f = 2$ and the angle between two families of fibers is given by 2γ .

4.1 Cantilever bending

As shown in Fig. 2.a, a cantilever strip, with $L \times W \times T = 10 \times 3 \times 0.3$ [mm³], is subjected to a distributed vertical force on its free end. The cantilever is meshed by 6×18 quadratic NURBS-based elements (see Fig. 2.b). It is assumed that the composite shell is composed of 5 symmetric layers laminated as shown in Fig. 1.b. The layers are distributed equally through the shell thickness T such that the thickness of each layer is $T/5$. The material properties vary layer-wise as listed in Table 1. The angle γ is measured w.r.t. the longitudinal direction.

Layer # i	T_i [T]	\tilde{c}_1 [kPa]	\tilde{c}_2 [kPa]	\tilde{c}_{3j} [kPa]	γ [deg]
1	0.1	30	120	600	± 60
2	0.3	20	60	1000	± 45
3	0.5	10	20	1000	± 30

Table 1: Material properties of the laminated composite cantilever.

Fig. 2.b shows the deformed configuration colored by $I_1 := \text{tr } \mathbf{C}$. As can be observed, I_1 slightly deviates from 2, which is the expected value for the case of pure bending. Further, there is transverse bending in the strip (like a saddle) due to the incompressibility of material. As shown in Fig. 2.c, both DD and NP shell models predict the same deflection for the cantilever tip. The total force applied on the cantilever tip is normalized by $E I/L^2$, where $E = 3\tilde{c}_1$ and $I = T W^3/12$ is the second moment of area of the cross section. For the numerically-projected shell model, 2 Gaussian quadrature points are used for each laminate. As compared in Fig. 2.d for different mesh sizes, the directly-decoupled shell model is numerically less expensive and more efficient than the numerically-projected shell model; nevertheless, it is restricted to symmetric layers.

Moreover, the anisotropic material model (57) can be reduced to an isotropic one simply by neglecting the anisotropic term, i.e. by setting $\tilde{c}_{3j} = 0$. Fig. 3 shows the bending of the same cantilever of Fig. 2.a for this case. The corresponding material parameters are extracted from

Table 1, setting $\tilde{c}_{3j} = 0$. Like the anisotropic example, the directly-decoupled shell model is as accurate as the numerically-projected shell model.

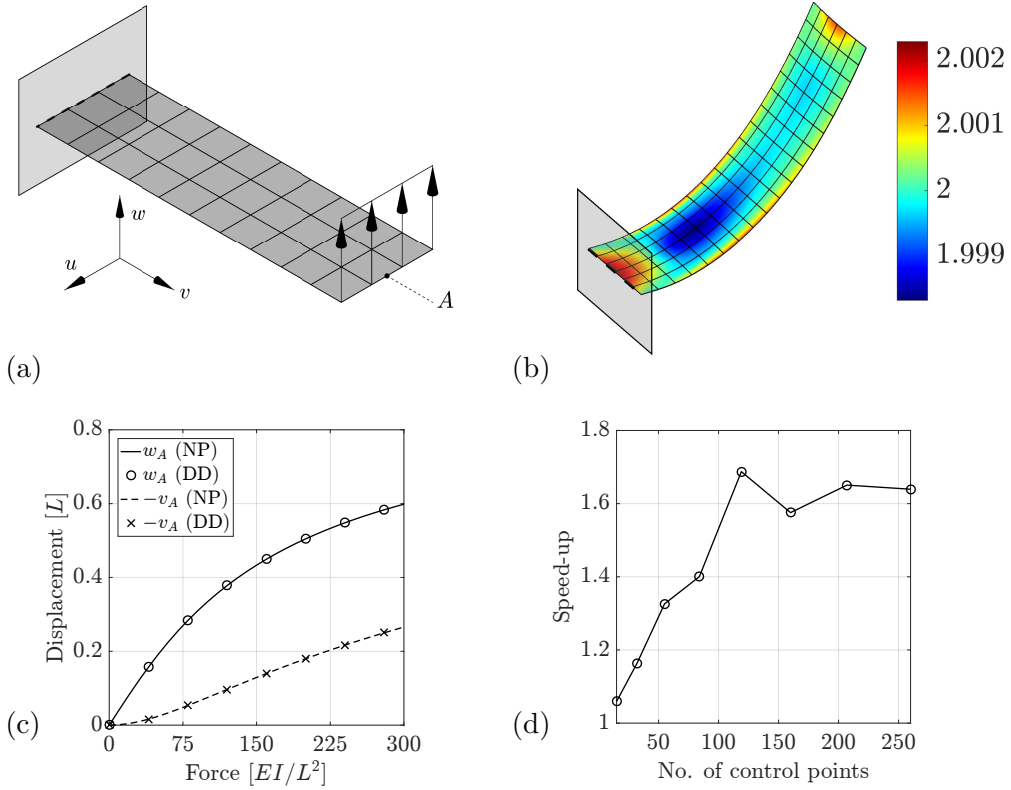


Figure 2: The cantilever bending test with anisotropic Mooney–Rivlin material model: (a) Undeformed configuration. (b) Deformed configuration colored by $I_1 := \text{tr } \mathbf{C}$. (c) Displacement of the tip vs. the total applied force. (d) Speed-up of the DD shell model w.r.t. the NP shell model.

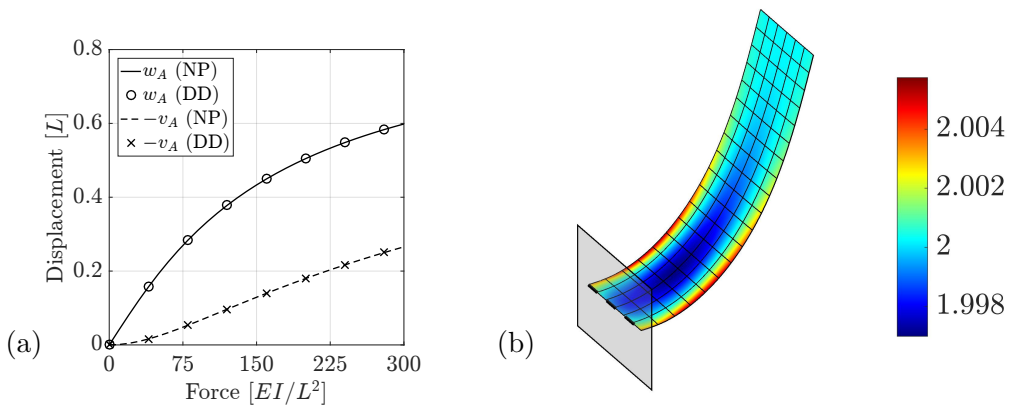


Figure 3: The cantilever bending test with isotropic Mooney–Rivlin material model: (a) Displacement of the tip vs. the total applied force. (b) Deformed configuration colored by $I_1 := \text{tr } \mathbf{C}$.

4.2 Clamped plate

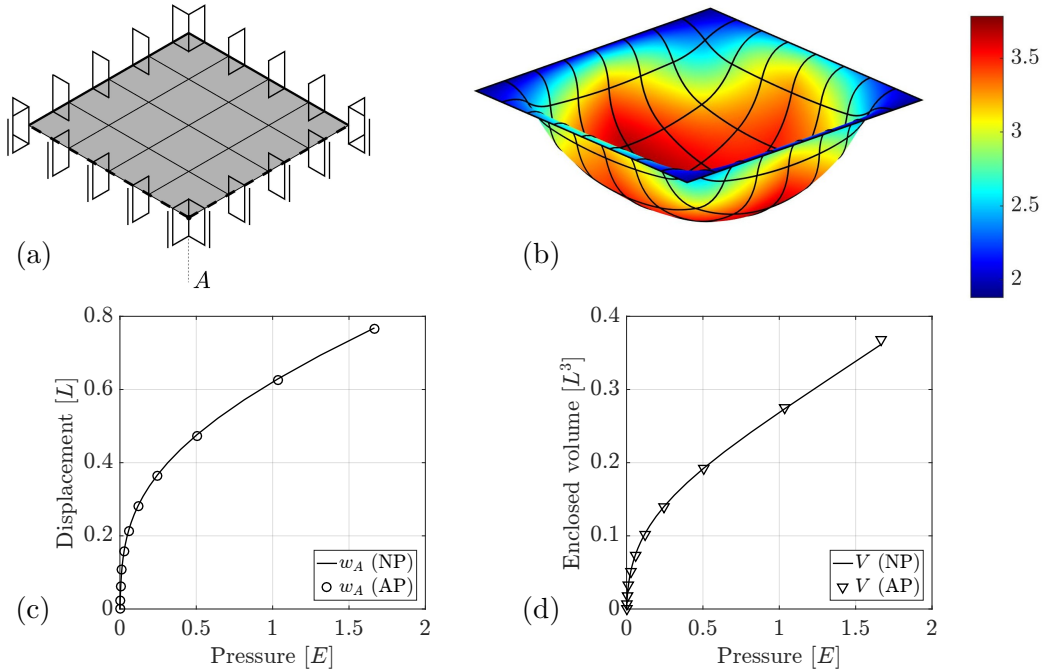


Figure 4: The clamped plate test with anisotropic Mooney–Rivlin material model: (a) Undeformed configuration (quarter system). The clamped edges and symmetric boundaries are denoted by thick solid and dashed lines, respectively. (b) Deformed configuration colored by $I_1 := \text{tr } \mathbf{C}$ (full system). (c) Displacement of the center point vs. the applied pressure. (d) Enclosed volume of plate vs. the applied pressure.

This example is designed to investigate the cases that both bending and membrane forces are dominant. Accordingly, a completely clamped square plate, with $L \times L \times T = 10 \times 10 \times 0.1$ [mm³], is loaded by an external live pressure. As depicted in Fig. 4.a, only a quarter of plate is modeled due to the symmetry of the problem. The rotation is fixed along the symmetry and clamped boundaries according to the penalty formulation of Duong et al. (2016). The plate is meshed by 4×4 quadratic NURBS-based elements as shown in Fig. 4.a. The plate constitution is modeled by the incompressible anisotropic Mooney–Rivlin material model of Eq. (57). Now, the laminates are not symmetric w.r.t. the shell mid-surface (see Table 2). The orientation of fibers is defined by the angle γ measured w.r.t. the right symmetry edge (see Fig. 4.a). Here, the analytical and numerical projection approaches are compared. For the NP shell model, 2 Gaussian quadrature points are considered for each laminate layer. As shown in Figs. 4.c and 4.d, the results of AP and NP shell models are in excellent agreement.

Layer # i	T_i [T]	\tilde{c}_1 [kPa]	\tilde{c}_2 [kPa]	\tilde{c}_{3j} [kPa]	γ [deg]
1	-0.35	20	60	200	± 15
2	0.10	15	30	75	± 30
3	0.20	30	30	60	± 45
4	0.40	25	50	125	± 60
5	0.50	10	20	100	± 75

Table 2: Material properties of the laminated composite plate.

4.3 Pressurization of a tube

As shown in Fig. 5, a laminated composite tube, with $L \times R \times T = 20 \times 5 \times 0.25$ [mm³], is pressurized by the live pressure p_{ext} . It is assumed that the tube is constructed from 5 layers as listed in Table 2; however, here the fiber directions are measured w.r.t. the axial direction. As the problem is symmetric, only 1/8 of tube is modeled (see Fig. 5.a) and the symmetry boundary conditions are applied accordingly using the constraint of Duong et al. (2016). On the tube end, three different boundary conditions are considered: (1) Free end, (2) closed end, where the tensile traction $p_{\text{ext}} R/2T$ is applied along the axial direction, and (3) fixed end, where all the displacements are restricted. Furthermore, for the first two cases, the rotations on the tube end are fixed by the constraint of Duong et al. (2016).

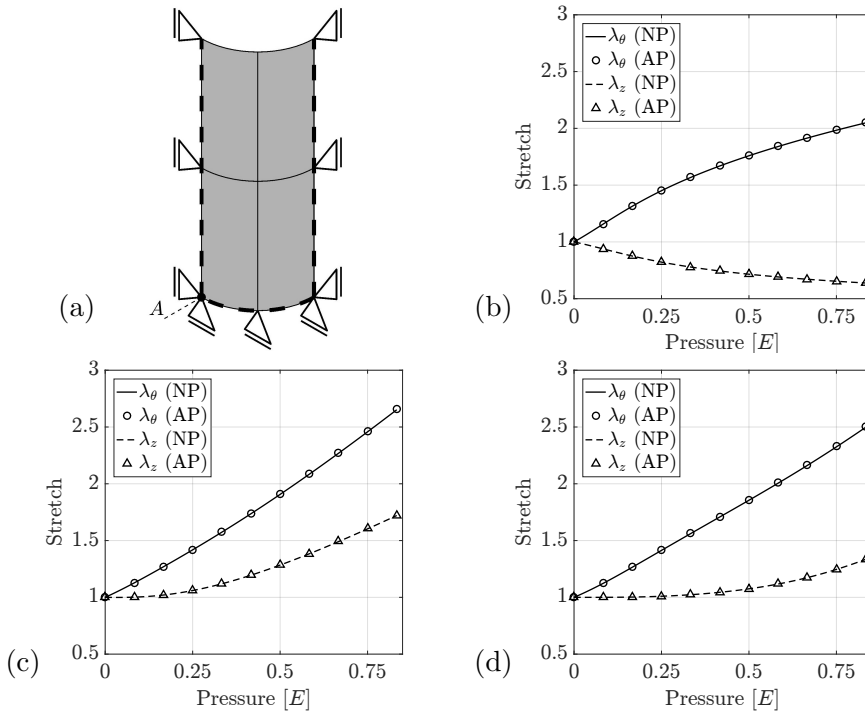


Figure 5: The tube test with anisotropic Mooney–Rivlin material model: (a) Undeformed configuration (quarter system). The symmetric boundaries are denoted by thick dashed lines. Circumferential stretch λ_θ and axial stretch λ_z of the tube with (b) free end, (c) traction on the end and (d) fixed end.

As shown in Figs. 5.b-d, the circumferential stretch λ_θ and axial stretch λ_z of the tube are predicted identically by both the NP and AP shell models. The stretches λ_\bullet are calculated at the middle point A shown in Fig. 5.a. The applied pressure is normalized by $E = 3 \tilde{c}_1$. Further, Fig. 6 shows the deformed tube for different boundary conditions. Using quadratic NURBS-based shape functions, for all cases, an accurate solution is obtained by the coarse 2×2 mesh shown in Fig. 5.a.

5 Conclusion

Three different approaches to model thin laminated composite shells based on the Kirchhoff–Love hypothesis are presented, namely the *numerically-projected* (NP), *analytically-projected*

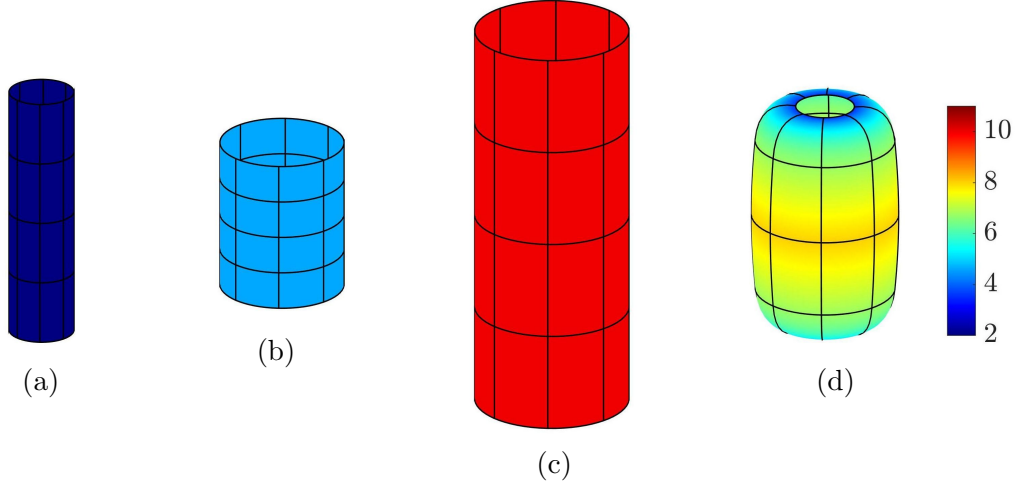


Figure 6: The pressurized tube colored by $I_1 := \text{tr } \mathbf{C}$ (full system): (a) Undeformed configuration and deformed configurations ($p_{\text{ext}} = 0.83 E$) for the tube with (b) free end, (c) traction on the end and (d) fixed end.

(AP) and *directly-decoupled* (DD) shell models. The proposed models are suitable for thin rotation-free shells and they are formulated in the framework of equivalent single layer (ESL) theory. Further, the kinematics are adopted from classical laminated plate theory. Beside the Kirchhoff–Love assumptions, it is assumed that: (1) the layers are perfectly bonded together, (2) each layer is of uniform thickness, (3) the material can have any desired nonlinear isotropic or anisotropic constitution and (4) the strains and deformations can be arbitrarily large.

The numerically-projected shell model is the most general one, which can be used to analyze composite shells with any desired constitution and laminate arrangement. However, it generally requires numerical integration through the shell thickness. In fact, for each individual laminate layer, separate integration is needed, which can be computationally expensive. If the shell thickness is considerably smaller than the other dimensions or curvature radii of the shell, the analytically-projected shell model can be used, which is computationally more feasible as it does not need any numerical through-the-thickness integration. For laminated composite shells that have symmetric arrangement and material properties w.r.t. the shell mid-surface, one can use the directly-decoupled shell model. This approach is the most efficient one; however, it is restricted to symmetric shells.

The presented shell models can be used to analyze any arrangement and material behavior of the layers. The FE solution is based on isogeometric analysis (IGA) and quadratic NURBS-based elements are used to ensure the smoothness required for the analysis of thin shells. The robustness and accuracy of the formulation is shown by several numerical examples, which examine the mixed membrane and bending modes of deformation.

The current formulation assumes that the laminated layers are perfectly bonded. In the future, one can also account for delamination and inter-layer contact. Further, the model can be modified according to layer-wise and higher order shear deformation theories to analyze thicker shells or plates.

Acknowledgement

Financial support from the German Research Foundation (DFG) through grant GSC 111, is gratefully acknowledged.

References

- Aragh, B. S., Barati, A. N., and Hedayati, H. (2012). Eshelby–Mori–Tanaka approach for vibrational behavior of continuously graded carbon nanotube-reinforced cylindrical panels. *Composit. Part B: Engrg.*, **43**(4):1943–1954.
- Bazilevs, Y., Deng, X., Korobenko, A., di Scalea, F. L., Todd, M., and Taylor, S. (2015). Isogeometric fatigue damage prediction in large-scale composite structures driven by dynamic sensor data. *J. Appl. Mech.*, **82**(9):091008.
- Bazilevs, Y., Hsu, M.-C., Kiendl, J., Wüchner, R., and Bletzinger, K.-U. (2011). 3D simulation of wind turbine rotors at full scale. Part II: Fluid–structure–interaction modeling with composite blades. *Int. J. Num. Meth. Fluids*, **65**(1-3):236–253.
- Borden, M. J., Scott, M. A., Evans, J. A., and Hughes, T. J. R. (2011). Isogeometric finite element data structures based on Bezier extraction of NURBS. *Int. J. Numer. Meth. Engrg.*, **87**:15–47.
- Carrera, E. (2002). Theories and finite elements for multilayered, anisotropic, composite plates and shells. *Arch. Comput. Meth. Engrg.*, **9**(2):87–140.
- Carrera, E. and Brischetto, S. (2009). A survey with numerical assessment of classical and refined theories for the analysis of sandwich plates. *App. Mech. Rev.*, **62**(1):010803.
- Casanova, Cesar F.; Gallego, A. (2013). NURBS-based analysis of higher-order composite shells. *Compos. Struct.*, **104**:125–133.
- Cottrell, J. A., Hughes, T. J. R., and Bazilevs, Y. (2009). *Isogeometric analysis: Toward integration of CAD and FEA*. Wiley, Chichester, West Sussex, UK.
- Deng, X., Korobenko, A., Yan, J., and Bazilevs, Y. (2015). Isogeometric analysis of continuum damage in rotation-free composite shells. *Comp. Meth. Appl. Mech. Engrg.*, **284**:349–372. Isogeometric Analysis Special Issue.
- Duong, T. X., Roohbakhshan, F., and Sauer, R. A. (2016). A new rotation-free isogeometric thin shell formulation and a corresponding C^1 -constraint for patch boundaries. *Comp. Meth. Appl. Mech. Engrg.*, doi:10.1016/j.cma.2016.04.008.
- Eshelby, J., Read, W., and Shockley, W. (1953). Anisotropic elasticity with applications to dislocation theory. *Acta metal.*, **1**(3):251–259.
- Eshelby, J. D. (1957). The determination of the elastic field of an ellipsoidal inclusion, and related problems. In *Proceedings of the Royal Society of London A: Mathematical, Physical and Engineering Sciences*, volume **241**, pages 376–396. The Royal Society.
- Guo, Y. (2016). *Isogeometric analysis for thin-walled composite structures*. TU Delft, Delft University of Technology, Enschede, The Netherlands.
- Guo, Y., Nagy, A. P., and Gürdal, Z. (2014a). A layerwise theory for laminated composites in the framework of isogeometric analysis. *Compos. Struct.*, **107**:447–457.
- Guo, Y. and Ruess, M. (2015). A layerwise isogeometric approach for NURBS-derived laminate composite shells. *Compos. Struct.*, **124**:300–309.
- Guo, Y., Ruess, M., and Gürdal, Z. (2014b). A contact extended isogeometric layerwise approach for the buckling analysis of delaminated composites. *Compos. Struct.*, **116**:55–66.

- Hosseini, S., Remmers, J. J., Verhoosel, C. V., and Borst, R. (2015). Propagation of delamination in composite materials with isogeometric continuum shell elements. *Int. J. Numer. Meth. Engrg.*, **102**(3-4):159–179.
- Hosseini, S., Remmers, J. J., Verhoosel, C. V., and de Borst, R. (2014). An isogeometric continuum shell element for non-linear analysis. *Comp. Meth. Appl. Mech. Engrg.*, **271**:1–22.
- Hughes, T. J. R., Cottrell, J. A., and Bazilevs, Y. (2005). Isogeometric analysis: CAD, finite elements, NURBS, exact geometry and mesh refinement. *Comp. Meth. Appl. Mech. Engrg.*, **194**:4135–4195.
- Kapoor, H. and Kapania, R. (2012). Geometrically nonlinear NURBS isogeometric finite element analysis of laminated composite plates. *Compos. Struct.*, **94**(12):3434–3447.
- Kiendl, J., Bazilevs, Y., Hsu, M.-C., Wüchner, R., and Bletzinger, K.-U. (2010). The bending strip method for isogeometric analysis of Kirchhoff-Love shell structures comprised of multiple patches. *Comput. Methods Appl. Mech. Engrg.*, **199**(37-40):2403–2416.
- Kiendl, J., Bletzinger, K.-U., Linhard, J., and Wüchner, R. (2009). Isogeometric shell analysis with Kirchhoff-Love elements. *Comput. Methods Appl. Mech. Engrg.*, **198**:3902–3914.
- Kreja, I. (2011). A literature review on computational models for laminated composite and sandwich panels. *Open Engrg.*, **1**(1):59–80.
- Kreyszig, E. (1991). *Differential Geometry*. Dover, New York.
- Lei, Z., Liew, K. M., and Yu, J. (2013). Buckling analysis of functionally graded carbon nanotube-reinforced composite plates using the element-free kp-Ritz method. *Compos. Struct.*, **98**:160–168.
- Li, S. and Wang, G. (2008). *Introduction to micromechanics and nanomechanics*. World Scientific, Singapore.
- Lin, S.-Z., Zhang, L.-Y., Sheng, J.-Y., Li, B., and Feng, X.-Q. (2016). Micromechanics methods for evaluating the effective moduli of soft neo-Hookean composites. *Archive of Applied Mechanics*, **86**(1-2):219–234.
- Lyshevski, S. (2002). *MEMS and NEMS: Systems, Devices, and Structures*. Nano- and Microscience, Engineering, Technology and Medicine. CRC Press, Boca Raton, Florida.
- Mori, T. and Tanaka, K. (1973). Average stress in matrix and average elastic energy of materials with misfitting inclusions. *Acta metal.*, **21**(5):571–574.
- Naghdi, P. M. (1982). Finite deformation of elastic rods and shells. In Carlson, D. E. and Shields, R. T., editors, *Proceedings of the IUTAM Symposium on Finite Elasticity*, pages 47–103, The Hague. Martinus Nijhoff Publishers.
- Ochoa, O. O. and Reddy, J. N. (1992). *Finite element analysis of composite laminates*. Springer, Dordrecht.
- Qatu, M. S., Asadi, E., and Wang, W. (2012). Review of recent literature on static analyses of composite shells: 2000–2010. *Open J. Compos. Mater.*, **2**:61–86.
- Qatu, M. S., Sullivan, R. W., and Wang, W. (2010). Recent research advances on the dynamic analysis of composite shells: 2000–2009. *Compos. Struct.*, **93**(1):14 – 31.

- Reddy, J. (1989). On refined computational models of composite laminates. *Int. J. Numer. Meth. Engrg.*, **27**(2):361–382.
- Reddy, J. and Robbins, D. (1994). Theories and computational models for composite laminates. *Appl. Mech. Rev.*, **47**(6):147–169.
- Reddy, J. N. (2004). *Mechanics of laminated composite plates and shells: theory and analysis*. CRC press, Boca Raton, Florida.
- Reddy, J. N. (2006). *Theory and analysis of elastic plates and shells*. CRC Taylor & Francis distributor, Boca Raton, Florida.
- Roohbakhshan, F., Duong, T. X., and Sauer, R. A. (2016). A projection method to extract biological membrane models from 3D material models. *J. Mech. Behav. Biomed. Mater.*, **58**:90–104.
- Roohbakhshan, F. and Sauer, R. A. (2016). Efficient isogeometric thin shell formulations for soft biological materials. arXiv:1612.09087.
- Sauer, R. A. and Duong, T. X. (2015). On the theoretical foundations of solid and liquid shells. *Math. Mech. Solids*, doi:10.1177/1081286515594656.
- Sauer, R. A., Duong, T. X., and Corbett, C. J. (2014). A computational formulation for constrained solid and liquid membranes considering isogeometric finite elements. *Comput. Methods Appl. Mech. Engrg.*, **271**:48–68.
- Steigmann, D. J. (1999). On the relationship between the Cosserat and Kirchhoff-Love theories of elastic shells. *Math. Mech. Solids*, **4**:275–288.
- Stroh, A. (1958). Dislocations and cracks in anisotropic elasticity. *Philos. mag.*, **3**(30):625–646.
- Thai, C. H., Ferreira, A., Bordas, S., Rabczuk, T., and Nguyen-Xuan, H. (2014). Isogeometric analysis of laminated composite and sandwich plates using a new inverse trigonometric shear deformation theory. *Eur. J. Mech. A-Solid*, **43**:89–108.
- Thai, C. H., Ferreira, A., Carrera, E., and Nguyen-Xuan, H. (2013). Isogeometric analysis of laminated composite and sandwich plates using a layerwise deformation theory. *Compos. Struct.*, **104**:196–214.
- Thai, C. H., Nguyen-Xuan, H., Bordas, S., Nguyen-Thanh, N., and Rabczuk, T. (2015). Isogeometric analysis of laminated composite plates using the higher-order shear deformation theory. *Mech. Adv. Mater. Struct.*, **22**(6):451–469.
- Thomas, B. and Roy, T. (2015). Vibration and damping analysis of functionally graded carbon nanotubes reinforced hybrid composite shell structures. *J. Vibrat. Cont.*, doi:10.1177/1077546315599680.
- Vel, S. S. and Batra, R. (1999). Analytical solution for rectangular thick laminated plates subjected to arbitrary boundary conditions. *AIAA J*, **37**(11):1464–1473.
- Vel, S. S. and Batra, R. (2000). The generalized plane strain deformations of thick anisotropic composite laminated plates. *Int. J. Solids Struct.*, **37**(5):715–733.
- Vel, S. S. and Batra, R. (2001). Generalized plane strain thermoelastic deformation of laminated anisotropic thick plates. *Int. J. Solids Struct.*, **38**(8):1395–1414.

Yang, H. T. Y., Saigal, S., Masud, A., and Kapania, R. K. (2000). A survey of recent shell finite elements. *Int. J. Numer. Meth. Engng*, **47**:101–127.

Zhang, Y. and Yang, C. (2009). Recent developments in finite element analysis for laminated composite plates. *Compos. Struct.*, **88**(1):147–157.